

Ultrathin AgPt alloy nanorods as low-cost oxygen reduction reaction electrocatalysts in proton exchange membrane fuel cells

Fidiani, Elok; Thirunavukkarasu, Gnanavel; Li, Yang; Chiu, Yu-Lung; Du, Shangfeng

DOI:

[10.1039/D0TA02748K](https://doi.org/10.1039/D0TA02748K)

License:

None: All rights reserved

Document Version

Peer reviewed version

Citation for published version (Harvard):

Fidiani, E, Thirunavukkarasu, G, Li, Y, Chiu, Y-L & Du, S 2020, 'Ultrathin AgPt alloy nanorods as low-cost oxygen reduction reaction electrocatalysts in proton exchange membrane fuel cells', *Journal of Materials Chemistry A*, vol. 8, no. 23, pp. 11874-11883 . <https://doi.org/10.1039/D0TA02748K>

[Link to publication on Research at Birmingham portal](#)

General rights

Unless a licence is specified above, all rights (including copyright and moral rights) in this document are retained by the authors and/or the copyright holders. The express permission of the copyright holder must be obtained for any use of this material other than for purposes permitted by law.

- Users may freely distribute the URL that is used to identify this publication.
- Users may download and/or print one copy of the publication from the University of Birmingham research portal for the purpose of private study or non-commercial research.
- User may use extracts from the document in line with the concept of 'fair dealing' under the Copyright, Designs and Patents Act 1988 (?)
- Users may not further distribute the material nor use it for the purposes of commercial gain.

Where a licence is displayed above, please note the terms and conditions of the licence govern your use of this document.

When citing, please reference the published version.

Take down policy

While the University of Birmingham exercises care and attention in making items available there are rare occasions when an item has been uploaded in error or has been deemed to be commercially or otherwise sensitive.

If you believe that this is the case for this document, please contact UBIRA@lists.bham.ac.uk providing details and we will remove access to the work immediately and investigate.

Ultrathin AgPt Alloy Nanorods as Low-cost Oxygen Reduction Reaction Electrocatalysts in Proton Exchange Membrane Fuel Cells

Elok Fidiani,[†] Gnanavel Thirunavukkarasu,[‡] Yang Li,[†] Yulung Chiu,[‡] Shangfeng Du^{†*}

[†]School of Chemical Engineering, University of Birmingham, Birmingham, B15 2TT, U.K.

[‡]School of Metallurgy and Materials, University of Birmingham, Birmingham, B15 2TT, U.K.

*To whom correspondence should be addressed. Email: s.du@bham.ac.uk (SD)

Abstract

The excellent catalytic activities and stabilities of one-dimensional (1D) AgPt alloy nanostructure have been well reported toward oxygen reduction reaction (ORR). However, their real application in proton exchange membrane fuel cells (PEMFCs) is still highly challenging due to the large difficulties with their preparation and fabrication into practical electrodes. By a facile self-growth assisted reduction method, ultrathin single-crystal AgPt alloy nanorods (NRs) with a diameter of 3-4 nm are uniformly grown on carbon support through a finely controlled ion reduction process tuning the nucleation and growth of Pt and Ag. Enhanced power performance is successfully demonstrated in the single-cell test. With 50 at% Ag, the AgPt NR/C electrode shows 1.16-fold power density and 1.22-fold mass activity over the Pt NR/C electrode, and 1.14 and 1.51-fold to the commercial Pt/C electrode, respectively. Comparable durability is also established in fuel cells by using the accelerated degradation test, although Ag is included.

Introduction

Known as the most efficient metal in accelerating oxygen reduction reaction (ORR) process at low temperature, platinum (Pt) has been employed as a standard ORR catalyst in acidic proton exchange membrane fuel cells (PEMFCs) ¹. To reduce the high cost from using Pt, the recent researches in developing the ORR catalysts have been intensively directed to the reduction of Pt loading, and the development of Pt-based alloy nanostructures has been demonstrated as a promising strategy ^{2,3}. Currently, the carbon black-supported Pt (Pt/C) catalysts in the form of zero-dimensional (0D) nanoparticles (NPs) with a diameter of 3-5 nm are used as the standard ORR catalysts in the cathodes of PEMFCs. However, poor stability during the fuel cell operation is a critical issue for these NP catalysts. The dissolution of small particles leads to Ostwald ripening, which is described as a process of redepositing the dissolved smaller particles onto the larger particles, together with the agglomeration susceptibly occurred among NPs, finally reducing the available catalyst surface resulting in the low catalytic activities ⁴. To address these challenges, a deliberate modification of the morphology of Pt based-catalysts is required, in particular, tailoring novel nanostructures with a high aspect ratio and a low number of the surface defect sites to develop highly stable catalysts in the fuel cell operation.

The development of one-dimensional (1D) nanostructure electrocatalysts such as nanowires (NWs), nanotubes (NTs) and nanorods (NRs) has been favored to address the challenges with 0D NPs ⁵⁻⁸. According to Koenigsmann et al., Pt-based single-crystal NWs possess significantly high activities toward ORR ⁹. Also, the defect-free surfaces of these nanostructures are expected to impart the enhanced stability towards the dissolution and ripening, thereby making them suitable for long-term use ¹⁰. The highlight of the development and performance of 1D nanostructure electrocatalysts for PEMFCs has also been reviewed recently, resuming the impressive progress

in the design and synthesis of 1D nanomaterials as the active and durable electrocatalysts for PEMFCs ¹¹.

The integration of Pt with the different metals has also been long studied to reduce the Pt loading and improve the catalyst performance ¹²⁻¹⁴. Alloying Pt to form bimetallic or intermetallic catalysts potentially increases the ORR activity by modifying the electronic structure of the surface Pt ¹⁵. Besides, the addition of less expensive metals will bring an advantage in economic benefit. To this end, Pt has often been alloyed with the transition metals such as Ni, Fe, and Co ¹⁶⁻¹⁸. However, these base metal alloys are highly susceptible towards the oxidation which accelerates the catalyst degradation and inducing poor stability for long term use ^{19,20}.

Noble metals such as Pd, Au and Ag are still favorable alloyed candidates for Pt to achieve excellent stability because of their high resistance against oxidation. Among the noble metals, with a price similar to Co and less than 2% of Pt, Ag is very popular as a candidate, especially in the alkaline media ²¹. Furthermore, due to the similar ORR kinetics and reaction mechanisms of Ag and Pt in alkaline, alloying Ag with Pt also incurs an advantage for the enhanced catalytic activities ²². In the form of 1D nanostructures, Liang et al. resumed the ORR activities of Pt@M (M = Au, Ag and Pd) core-shell nanorods, reporting that Pt@Ag NRs showed the highest stability in 0.5 M HClO₄ ²³. In recent studies, the excellent catalytic activities have also been reported by controlling PtAg alloy to form NWs, nanochains, and nanotrees ²⁴⁻²⁶. However, most of these approaches remain in the ex-situ half-cell electrochemical measurement in the liquid electrolytes. The complex fabrication processes and large difficulties in fabricating them into practical electrodes (because of anisotropic morphology) arise as the hindrances to move these novel 1D alloy nanostructured catalysts forward to the practical application in fuel cells. Although the ex-situ measurement is substantial to define the catalyst activities, the affirmation of the catalyst performance in practical

fuel cells is crucial to attenuate the barriers for commercialization, as the catalysts can encounter profoundly different severe conditions in the PEMFCs operation ^{27,28}.

In an attempt to address these limitations, this work focuses on the three aspects: (i) designing a facile method to synthesize 1D AgPt alloy ORR catalysts highly transferable to fuel cells. The capping agent such as polyvinylpyrrolidone (PVP) for directing the formation of 1D nanostructures is eliminated in this method, as it potentially interferes with the catalyst activities in fuel cells ²⁹. Instead, formic acid is utilized as a reducing and directing agent. A self-growth assisted formic acid reduction method has been well reviewed for the synthesis of monometallic 1D Pt nanostructures, however, rarely applied for the bimetallic structures ³⁰. Therefore, a broad synthesis mechanism is comprehensively investigated in this study for the scale-up preparation for the practical application purpose; (ii) Performing the membrane electrode assembly (MEA) testing in single-cell PEMFCs to better understand the behavior of 1D AgPt alloy in the fuel cell operation condition; and (iii) Pt alloy catalysts often emerge with the stability issues especially under the complex and harsh operating conditions in fuel cells, particularly with Ag. Hence, the accelerated degradation test (ADT) is also conducted in single-cell PEMFC test to understand the degradation behavior of the as-prepared AgPt NR catalysts.

Experimental

Materials

Carbon black Vulcan XC-72R was purchased from FuelCellStore (USA). H_2PtCl_6 (8 wt% in H_2O), 0.1 M AgNO_3 and HCOOH ($\geq 95\%$) were used as received from Sigma-Aldrich (UK). Ethanol and 2-propanol (IPA) were supplied from Fisher Scientific (UK). 10 wt% Nafion®

polymer dispersion (D1021) was obtained from Ion Power Inc. (USA). Pt/C catalyst (46.2 wt% Pt, TEC10E50E, TKK, Japan) was used as the benchmark catalyst for the in-situ PEMFCs test.

Growing AgPt alloy nanorods on carbon

For a typical synthesis of AgPt NR/C (1:1) (atomic ratio of Ag:Pt = 1:1), 50 mg of carbon black was dispersed in 100 mL of DI water using bath sonication (the water used was deionized (DI) to 18 M Ω cm using a Millipore water system, Milli-Q). 1 mL of H₂PtCl₆ (8 wt% in H₂O) in 50 mL of DI water was added subsequently to the carbon suspension, followed by adding 10 mL of HCOOH dropwise. After 5 hours, 2 mL of 0.1 mol L⁻¹ AgNO₃ in 50 mL of DI water was added under stirring. The solution was then left at room temperature (RT) for a total duration of 96 hours to finish the reaction. The washing step was undertaken three times with DI water and ethanol using a centrifuge, followed by drying in the oven (60 °C, 2h). The catalyst was finally heat-treated at 120 °C for 2 h under 60 mL min⁻¹ of 4% H₂/Ar within a quartz tube in a tube furnace (Vecstar Ltd., UK). To synthesize catalysts with the various AgPt metal ratios, the varied amount of Pt and Ag precursors was applied, but the total amount was kept the same.

Physical characterization

The structure information and chemical feature of the catalysts were characterized using a transmission electron microscope (TEM) (JEOL 1400 TEM, 80 kV) and a high-resolution scanning transmission electron microscope (HR-STEM, Talos F200X) operating at 200 kV with which the elemental mapping was carried out using the associated super-X EDS system with four silicon drift detectors (SDDs) (Bruker, USA). Scanning electron microscope conducted with energy-dispersive X-ray spectroscopy (SEM-EDX, Hitachi TM3030) was also used to analyze the

cross-sectional element mapping. Thermogravimetric analysis (TGA) was conducted with NETZSCH TG209F1 (Germany) between 20-900 °C to estimate the metal loading on carbon and the information of thermal stability of the catalysts. The element content of the catalysts was analyzed using inductively coupled plasma mass spectrometry (ICP-MS, Perkin Elmer Nexion 300X, USA) with a plasma strength of 1500 W. Powder X-ray diffractometer (XRD, D8 Bruker) equipped with a Cu K α X-Ray source ($\lambda = 0.15406$ nm) was used to understand the crystal structure of the catalysts. X-ray photoelectron spectroscopy (XPS) analysis was conducted using Thermo Fisher Scientific NEXSA spectrometer with a micro-focused monochromatic Al K α source (72 W). All XPS data analysis was performed using the CasaXPS software (version: 2.3.18PR1.0), and the sample charging was corrected using C 1s peak at 284.8 eV as reference.

MEA fabrication and fuel cell testing

The as-prepared catalysts with a loading of 0.2 mg_{Pt} cm⁻² were dispersed into 0.5 mL of IPA containing 45.7 μ L of 10wt% Nafion[®] solution for making catalyst ink, which was then painted onto a piece of 4 \times 4 cm² Sigracet 35BC GDL and then left to dry for 2 hours at 35°C (**This low dry temperature was used for reducing cracks formed across the catalyst layer with GDEs while balancing the drying time.**). Commercial gas diffusion electrodes (GDEs, 0.2 mg_{Pt} cm⁻², FuelCellStore USA) were used as anodes for all MEAs. The MEA was fabricated by assembling the cathode with the as-prepared catalysts, 6 \times 6 cm² Nafion[®] 212 membrane and the commercial anode, then hot pressed at 135 °C under an 1800 lb load for 2 minutes. The MEA was allowed to cool down at room temperature before testing in PEMFCs.

The MEA was tested using a Biologic-PaxiTech FCT-50S PEM fuel cell test rig (France) with polytetrafluoroethylene (PTFE, 254 μ m in thickness) gaskets used at both the anode and cathode

sides. The MEA activation (membrane hydration) was carried on at 0.6 V for 12-14 hours to reach a stable current at a cell temperature of 80 °C with fully humidified H₂/air at an absolute pressure of 1.5/1.5 bar and stoichiometric ratios of 1.3/1.5, respectively. Polarization curves were then recorded following the harmonized EU protocols with H₂ and air at absolute pressures of 2.5/2.3 bar, respectively. The electrochemical impedance spectroscopy (EIS) measurement was conducted in the frequency range of 10 kHz–0.1 Hz at 0.03 A cm⁻² and 0.5 V with an amplitude of 72 mA and 10 mV, respectively (0.5 V rather than a large current density was selected here because for some poor catalysts/GDEs, a large current density (e.g. 1.0 A cm⁻²) could not be reached.).

For ORR mass activity evaluation in the MEA, the test was carried out with the same condition as in H₂/air testing however the cathode gas was switched to O₂ and the stoichiometry ratio of anode/cathode was changed to 2/9.5 with an absolute pressure of 1.5/1.5 bar respectively. The corrections were conducted to the resistance loss taken by running EIS at high frequency. Meanwhile, the H₂-crossover current was obtained by holding the potential at 0.5 V with cathode fully saturated under N₂ for 30 minutes. The cathode cyclic voltammetry measurement was then performed using EZStat-Pro (NuVant Systems Inc., USA) between 0.05-1.2 V with a scan rate of 20 mV s⁻¹, which is further used to measure the electrochemical surface area (ECSA). Additionally, the ADT of the cathodes was performed with 5000 potential sweep cycles between 0.6-1.2 V at a scan rate of 100 mV s⁻¹ to understand the stability of the catalysts in the fuel cell environment. The polarization curves and CVs were recorded after the ADT to compare with the initial power performance and ECSA in PEMFCs.

Results and Discussion

In this work, AgPt alloy NRs were grown on the carbon support in the aqueous solution using hexachloroplatinic acid and silver nitrate as the metal precursors. Based on the slow reaction rate to configure 1D Pt nanostructure with formic acid as a reducing agent, the modified aqueous conditions have been used to derive the crystal nucleation and growth of both Pt and Ag on the carbon support³¹. In the formic acid reduction process, the parameters such as the reaction temperature and duration play the essential roles in the formation of 1D Pt nanostructures with a high crystallinity^{30,32}. Considering this condition, a good understanding of the influence mechanisms of the reaction temperature and duration is important in this work, in order to restrain the kinetic rate and interaction of Ag and Pt in the aqueous solution.

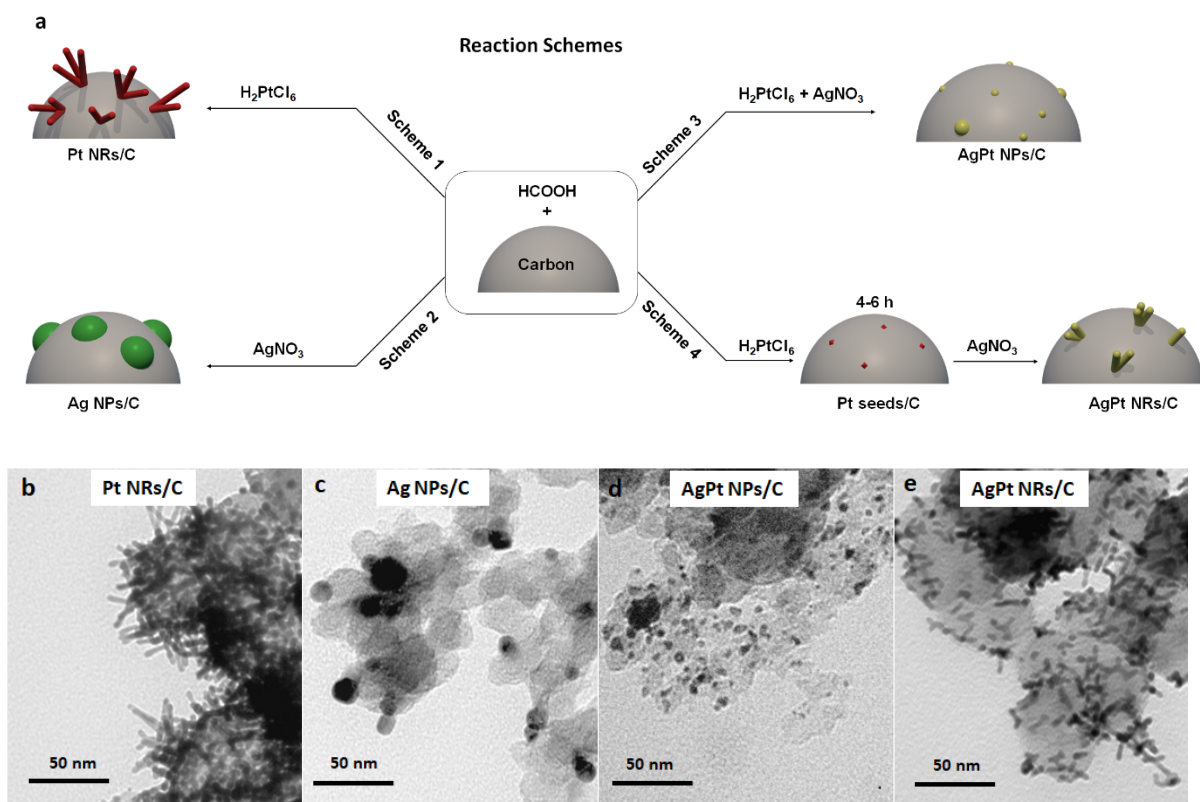


Fig. 1 a) The reaction schemes of Pt and Ag growth on the supported carbon black conducted at room temperature with a total reaction duration of 96 hours. **b-e)** TEM images of the catalysts obtained from reactions shown in Schemes 1-4 in (a).

The reaction mechanisms are schematically illustrated in **Fig. 1a**. In the aqueous formic acid-reducing process, the metal salts are reduced by formate anion species produced from the dehydration of formic acid. This dehydration process is favoured on the Pt surface except for Pt [111] crystal facet³³. Thus, with the balance of undissociated formic acid and formate anion species, the system condition automatically assists the growth of Pt along the <111> direction to form 1D nanostructures. This growth has been widely reported and is illustrated in Scheme 1 with the TEM image of the catalyst shown in **Fig. 1b**. Pt and Ag ions have very close standard reduction potential (SHE) ($E^0_{(Pt(+IV)/Pt(+II))} = 0.68$ V vs SHE; $E^0_{(Pt(+II)/Pt(0))} = 0.75$ V vs SHE, and $E^0_{(Ag(+)/Ag(0))} = 0.79$ V vs SHE). So, the formate anion is also able to reduce Ag^+ into Ag metal at room temperature. However, it cannot control the formation of Ag NPs along a specific direction due to the less attraction of Ag surface towards formate anion species compared to Pt. As a consequence, in the absence of Pt ions, the conformation of large Ag nanoparticles is inevitable as shown in Scheme 2 and **Fig. 1c**. When Pt and Ag precursors are mixed together from the beginning of the reaction, as the formation of Ag NPs dominates the early stage of the reaction (due to the faster reduction rate of Ag ions), the large agglomerates of NPs are still observed (Scheme 3 and **Fig. 1d**). Therefore, to facilitate the formation of 1D AgPt nanostructures, the whole process still needs to be dominated by Pt reduction. Considering the faster reduction rate of Ag ions (*cf.* Pt), it is necessary for Pt to be reduced at first to form crystal seeds to mediate the epitaxial growth of both metals into a specific direction. Due to the relative lower standard reduction potential of Pt ions (Pt^{4+} and Pt^{2+}) than that Ag^+ , a slower kinetic of Pt reduction is expected compared to Ag under the identical aqueous condition. Thus, Ag precursor is introduced to the reaction system after a controlled duration of Pt reduction (i.e. 5 hours). **In this case, the early reduction of Pt ions allows the formation of Pt seeds introducing the shape and size-controlled effect for further reduction,**

finally achieve 1D AgPt nanostructure with an average diameter of 3-4 nm and length of ~15 nm (Scheme 4, Fig. 1e for an atomic ratio of Ag:Pt = 1:1, for Ag₁Pt₁ NR/C).

A single NR for the Ag₁Pt₁ NR/C catalyst by the high-resolution TEM analysis (Fig. 2a) indicates the single-crystal feature of the 1D nanostructure with a lattice spacing of 0.23 nm, which is assigned to {111} planes between the bulk Pt (JCPDS: 04-0802) and Ag (JCPDS: 04-0783) (0.227 nm and 0.235 nm, respectively). The lattice orientation confirms the anisotropic growth of 1D nanostructure along the <111> direction. The element mapping analysis by STEM-EDX (Fig. 2c-e) shows the distribution of Ag and Pt along NRs. The good overlapping of both maps without a high content of Ag at the boundary confirms the alloy structure of the AgPt NR/C catalyst²⁶. The similar results are observed for the Ag₁Pt₄ NR/C catalyst with Ag to Pt atomic ratio of 1:4 (Fig. S1). The ICP-MS and SEM-EDX analyses were both performed to determine the elemental contents of the catalysts. The results are listed in Table S1 along with the TGA data, showing a good consistency with the expected metal ratios deposited on carbon.

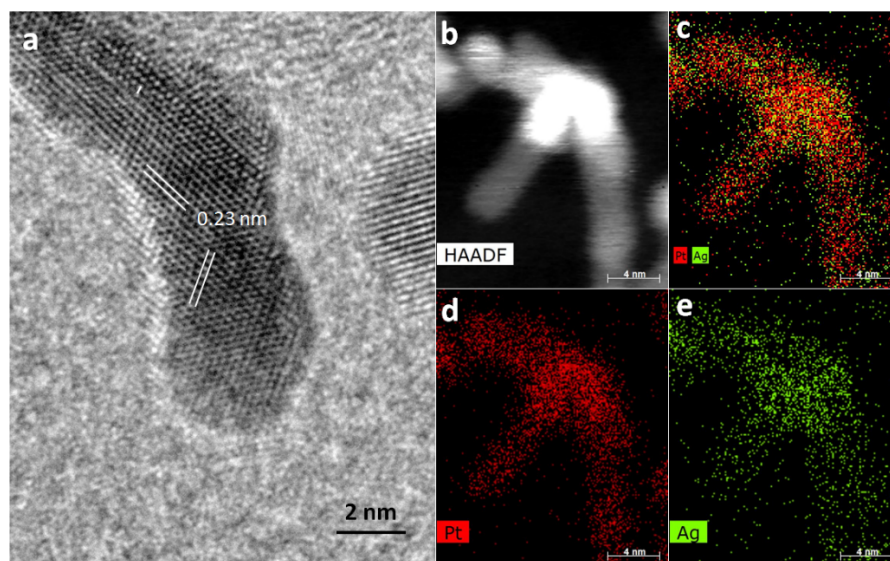


Fig. 2 a) High-resolution TEM image of Ag₁Pt₁ NR/C (atomic ratio of Ag:Pt = 1:1), **b-e)** show the element mapping by STEM-EDX analysis.

The investigation on the influence of Ag content on the NR morphology is shown in Fig. S2. The introduction of Ag reduces the length of the 1D catalyst nanostructures, and it decreases with the increasing Ag, signifying a faster kinetic reaction with the less concentration of Pt ions. Finally, the formation of NPs dominates the catalyst with a higher atomic ratio of Ag (Ag:Pt = 2:1) (Fig. S2e). However, if the metal ratio of Ag:Pt is kept at 2:1 (Ag₂Pt₁ NR/C -ii catalyst) but the concentration of the metal precursors is doubled toward formic acid, the reaction rate can be slowed down and NRs are achieved again, as shown in the TEM image in Fig. S2f. The domination of NRs here probably results from the reduced Ag content in the formed alloy phase because a big part has been consumed in formation of AgCl phase (as detected by XRD shown in Fig. S4). The detailed mechanism can be possibly clarified with further experiments but beyond this work with a focus on the AgPt alloy NRs. This finding suggests that the parameters deployed for ion reduction method work effectively to form 1D alloy nanostructure with the optimum ratio of Ag:Pt = 1:1. Otherwise, the acid leaching and the high-temperature treatment, e.g. 250 °C are required to remove Cl formed in the high Ag content^{34,35}. However, treatment at high temperature leads to the morphology change of the NRs structure, as shown in Fig. S5 that even a treatment temperature of 150 °C induces the sintering of the 1D structures forming the large particles. Therefore, the heat treatment temperature of 120 °C was selected for all the AgPt NR/C catalysts to minimize the impurities and optimize the properties of the catalysts.

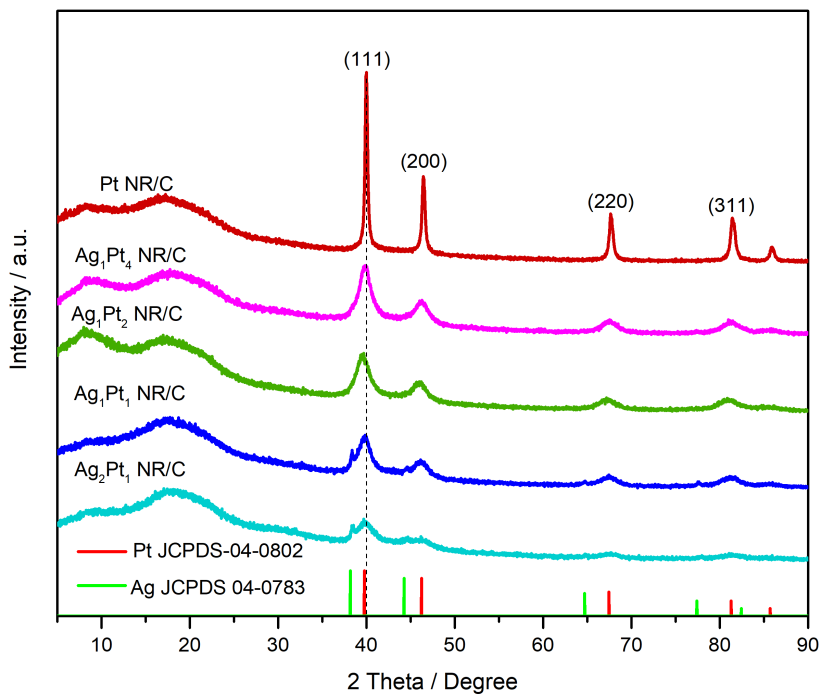


Fig. 3 XRD patterns of Pt NR/C and AgPt NR/C catalysts with the varied Ag and Pt atomic ratios.

XRD patterns of the AgPt NR/C catalysts with reference to Pt NR/C are shown in **Fig. 3**. The main peaks are well indexed to (111), (200), (220) and (311) crystal facets, appointed to the face-centred cubic (FCC) crystal structure. The measured lattice distance of Pt NR/C at (111) is 0.225 nm, which is close to the bulk Pt (JCPDS: 04-0802). The high peak intensity of Pt NR/C is addressed to the high crystallinity of the 1D nanostructure³⁶, which decreases with the introduction of Ag. This can be related to the lattice contraction caused by the different size of the Ag and Pt atoms and the reduced NR length, where, the similar XRD pattern behavior is also observed in the literature due to the change of concentration between Ag and Pt³⁷. The width of the XRD peaks is broader with the increasing of the Ag content, signifying the increased lattice effect and the size change (i.e. shorter NRs), which is in agreement with the TEM analysis (Fig. S2). The alloy with Ag also leads to the peak shift from Pt to Ag reference, and the (111) peak of the Ag₁Pt₂ NR/C catalyst shows a shift of 0.47 degree at two-theta compared to the Pt NR/C catalyst, corresponding

to an expanded lattice spacing of 0.228 nm. A further increase of the Ag content results in the formation of a separate Ag metal phase (e.g. with the AgPt NR/C (1:1) and Ag₂Pt₁ NR/C catalysts), which further indicates the complexity and limitation of using this formic acid reduction method for the preparation of 1D AgPt nanostructures.

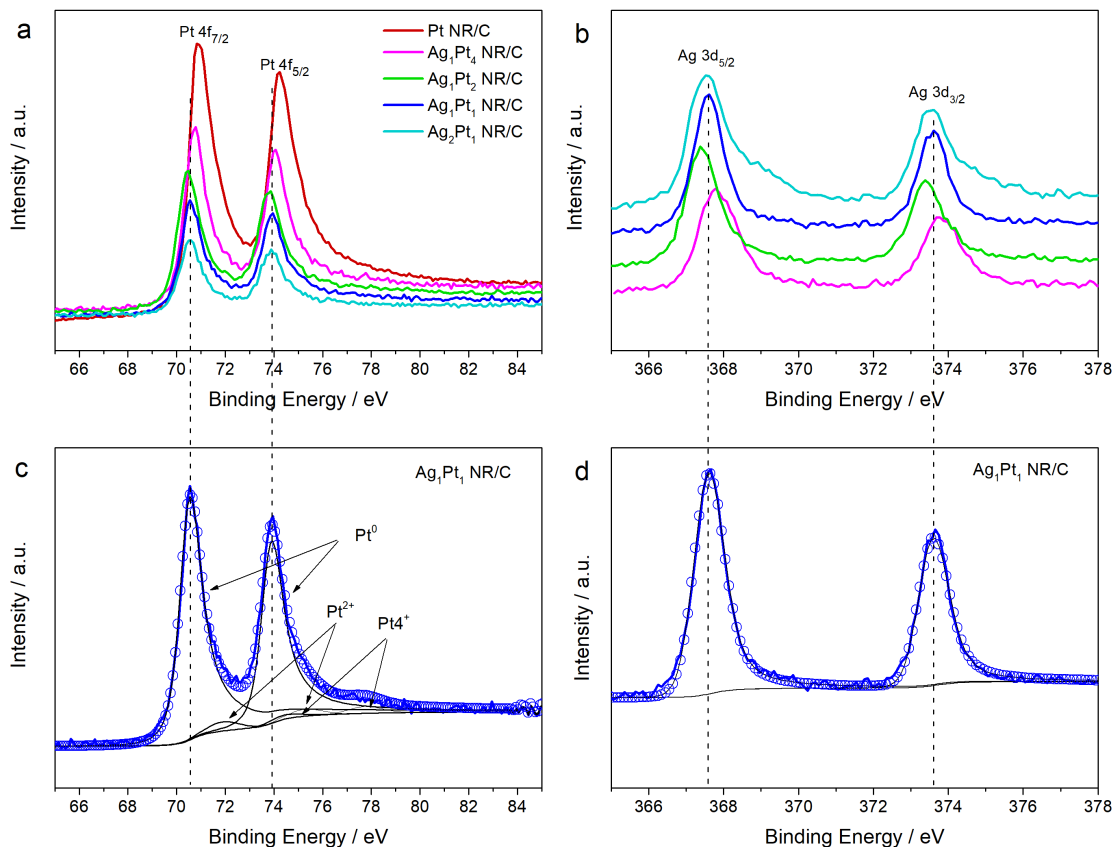


Fig. 4 XPS spectra of high-resolution a) Pt 4f and b) Ag 3d region of the Pt NR/C and AgPt NR/C catalysts. The band deconvolution for Ag₁Pt₁ NR/C given in the specific high-resolution XPS regions: c) Pt 4f and d) Ag 3d.

The X-ray photoelectron spectroscopy (XPS) analysis was conducted to understand the surface composition of the AgPt NR catalysts, and the survey scans are shown in Fig. S6. The high-resolution Pt 4f region of the Pt NR/C and AgPt NR/C catalysts with the varied Ag and Pt atomic

ratios are shown in **Fig. 4a**. The negative shift is clearly observed for the binding energy with a similar trend to the change in the XRD peaks (**Fig. 3**). A maximum negative shift of 0.41 eV is recorded for Pt 4f_{7/2} peak with the Ag₁Pt₂ NR/C catalyst relative to pure Pt (70.84 eV), and then the peak slightly shifts back with the increasing Ag content to 70.56 and 70.64 eV for Ag₁Pt₁ NR/C and Ag₂Pt₁ NR/C, respectively. The negative shift of the Pt peaks refers to the change of Pt-Pt binding energy induced by the change of the electronic structure of Pt because of the interaction with Ag³⁸. The same trend is also shown on the high-resolution Ag 3d spectrum with the largest shift observed at the atomic ratio of Ag to Pt = 1:2 (**Fig. 4b**), confirming the maximum lattice contraction with the atomic ratio of Ag:Pt=1:2. The negative shift of Ag 3d peaks observed is an indication of the charge transfer phenomena due to formation of the bimetallic Ag and Pt alloy, leading to the change of the binding energy of Ag metallic state ³⁹.

The peak fitting of Pt 4f spectrum for Ag₁Pt₁ NR/C (**Fig. 4c**) shows that Pt⁰ dominates the two peaks with a percentage of 94.08%, rendering the metallic state of Pt with ignorable the oxidation state of less than 6%. Regarding the high-resolution Ag 3d spectrum, Ag 3d_{5/2} and Ag 3d_{3/2} peaks locating at 367.66 and 373.70 eV, respectively, are wholly fitted to Ag⁰, confirming that Ag is effectively reduced to its metallic state (**Fig. 4d**). The Pt 4f and Ag 3d fitting results for the Pt NR/C and all the AgPt NR/C catalysts are summarized in Table S2, indicating the domination of Pt⁰ for all the NR catalysts (> 94%) and Ag⁰ for all the AgPt catalysts (> 97%). These results demonstrate the effectiveness of formic acid reduction method to form 1D Pt alloy NRs.

To understand the catalytic behavior of the as-prepared NR catalysts in the fuel cell operation, MEAs with Pt NR/C and AgPt NR/C as cathode catalysts were fabricated and tested in the H₂/Air single-cells with an active area of 16 cm². The gas diffusion electrodes (GDEs) were fabricated using the as-prepared Pt NR/C, AgPt NR/C and the benchmark Pt/C (TEC10E50E, TKK) catalysts

with the same Pt loading of $0.2 \text{ mg}_{\text{Pt}} \text{ cm}^{-2}$. The polarization and power density curves for all MEAs are shown in **Fig. 5a**. The similar open-circuit voltages (OCVs) are obtained for all MEAs at about 0.92 V. A very slightly lower peak power density is achieved for the MEA from the Pt NR/C catalyst (0.475 W cm^{-2}) than that of the Pt/C (0.483 W cm^{-2}), which is consistent with our work on the nanowire array GDEs³². When a small amount of Ag is introduced ($\text{Ag}_1\text{Pt}_4 \text{ NR/C}$), the peak power density shows a small decrease, which can be explained by the reduced NR length (Fig. S2) resulting in increased mass transfer losses, since the drop mainly exhibits at the large current density region. Meanwhile, with the significant increase of the Ag content, the peak power density becomes larger, and the maximum power density of 0.549 W cm^{-2} is achieved for the MEA with the $\text{Ag}_1\text{Pt}_1 \text{ NR/C}$ catalyst, which is 1.14-fold over that of Pt/C. The enhanced power density with the increase of Ag indicates a positive effect of Ag alloying toward the ORR catalytic activity. However, a further increase of Ag causes a big drop of the power performance, and the peak power density is only 0.428 W cm^{-2} for the MEA with the $\text{Ag}_2\text{Pt}_1 \text{ NR/C}$ catalyst. This outcome can be ascribed to the dominated nanoparticle morphology (Fig. S2e), losing the catalytic advantages of the 1D nanostructure catalysts.

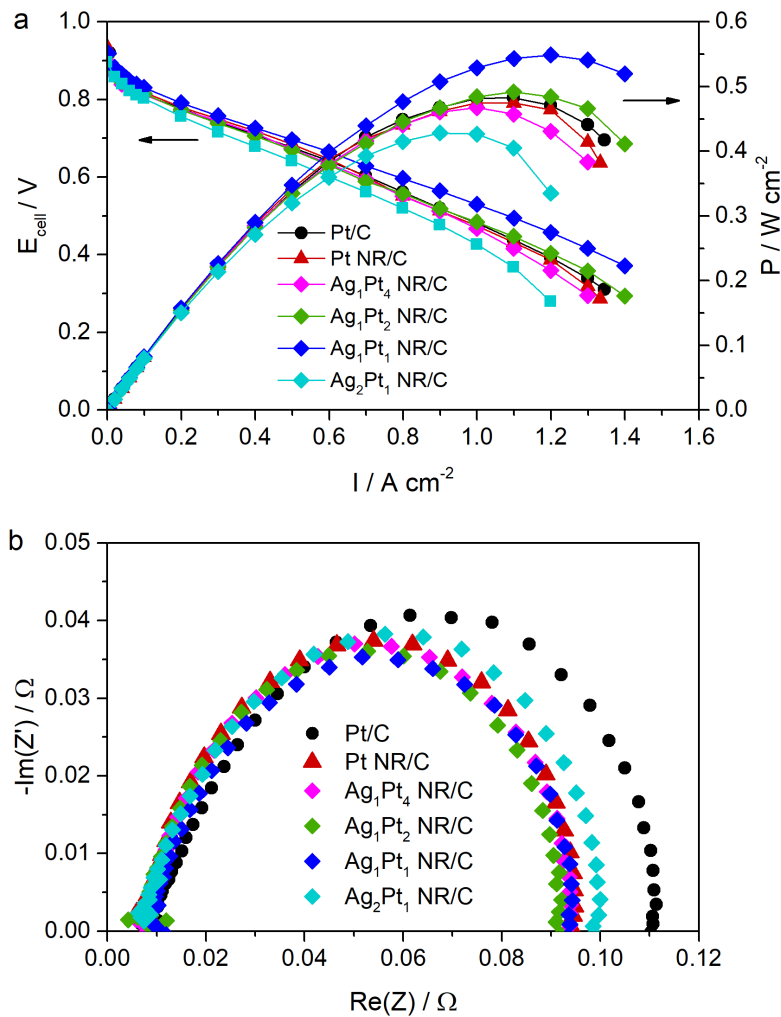


Fig. 5 MEA testing results of the as-prepared Pt NR/C and AgPt NR/C catalysts in comparison to Pt/C with the same Pt loading of $0.2\text{ mg}_{\text{Pt}}\text{ cm}^{-2}$: **a)** polarization and power density curves, and **b)** EIS plots recorded at 0.03 A cm^{-2} with an amplitude of 72 mA in the frequency range 10k–0.1 Hz. (the measurements were recorded at a cell temperature of $80\text{ }^{\circ}\text{C}$ and fully humidified H_2/air at a pressure of 2.5/2.3 bar with the stoichiometry of 1.3/1.5, respectively).

EIS analysis was conducted at 0.03 A cm^{-2} corresponding to the low current density region to further understand the catalytic behavior of the AgPt NR/C catalysts (**Fig. 5b**). At the low current density with high potential, the charge transfer resistance shown by the diameter of the semi-circle

are comparable for Pt NR/C, and AgPt NR/C with the different Ag contents of up to 50 at%, indicating a similar kinetic reaction rate. A larger charge transfer resistance is observed for Ag₂Pt₁ NR/C and Pt/C, confirming their relative low ORR activity. EIS measured at a low potential of 0.5 V (Fig. S7) shows the mass transport losses for the MEAs with different catalysts. Ag₁Pt₁ NR/C exhibits the lowest value, followed by Ag₂Pt₁ NR/C and Pt/C. In particular, at the low-frequency region, both NR catalysts show the lower impedance than Pt/C, further demonstrating the advantages of 1D nanostructure electrodes in reducing the mass transfer losses in operated fuel cells. The similar phenomena can also be observed for Ag₁Pt₄ NR/C and Pt NR/C. Despite a close impedance obtained at the high-frequency region for both catalysts, Pt NR/C still displays a smaller impedance than Ag₁Pt₄ NR/C at the low-frequency region because of the longer NR length (Fig. S2). The largest mass transfer losses are shown for Ag₂Pt₁ NR/C due to the dominated nanoparticle morphology. The trend for the charge and mass transfer resistances fully agrees with the change of the polarization curves shown in **Fig. 5a**. The improved power performance of the NR catalysts at the large current density (low potential) region can be firstly ascribed to the open catalyst layer structure afforded by the 1D NR catalysts enhancing gas transport through a smaller mean free path¹¹. Secondly, the improved electrical conductivity of the 1D metal nanostructures in addition to the inclusion of Ag provides the highest conductivity among the metals facilitating the electron transfer within the catalyst layer⁴⁰.

To understand the enhancement mechanisms of the heat treatment, a comparison with the MEAs made from the AgPt NR catalysts without the heat treatment is shown Fig. S8. It can be seen that the heat treatment improves the power performance for all MEAs with the AgPt NR catalysts, and the influence becomes large with the increase of the Ag content. A power increase of 6.6% is observed for the Ag₁Pt₁ NR/C catalyst. The TEM analysis shows the same NR structure upon

treatment at 120 °C (Fig. S5). XPS analysis results are compared in Fig. S9, with which Pt 4f peaks do not show any change, but Ag 3d peaks exhibit a tremendous positive shift of ca. 0.3 eV after the heat treatment. These phenomena are potentially related to the increase of Ag conductivity due to the heat treatment, suggesting the higher susceptibility of the heating process towards Ag property⁴¹. Finally, this reduces the charge transfer resistance and leads to improved electron transport throughout the catalyst layers.

The cathode cyclic voltammetry (CV) plots of the MEAs with the Pt/C, Pt NR/C and Ag₁Pt₁ NR/C catalysts are shown in **Fig. 6a**. The lower H₂ absorption/desorption (H_{ab}/H_{des}, below 0.4 V) peaks are observed for the 1D NR/C catalysts (*cf.* Pt/C) which is mainly caused by the 1D morphology of NRs leading to the decreased surface area. The electrochemical surface area (ECSA) obtained for the Pt NR/C catalyst is 14.68 m² g_{Pt}⁻¹, which is very close to the data reported in the previous study³². The alloying with Ag reduces the NR length (Fig. S2), and also leads to an increase in ECSA with a value of 24.26 m² g_{Pt}⁻¹ for the Ag₁Pt₁ NR/C catalyst, which further confirms the contributing factor in upgrading the power performance obtained in **Fig. 5a**. However, a higher atomic ratio of Ag (e.g. Ag:Pt = 2:1) induces the less exposure of the Pt active sites, resulting in a slightly reduced surface area (Fig. S10).

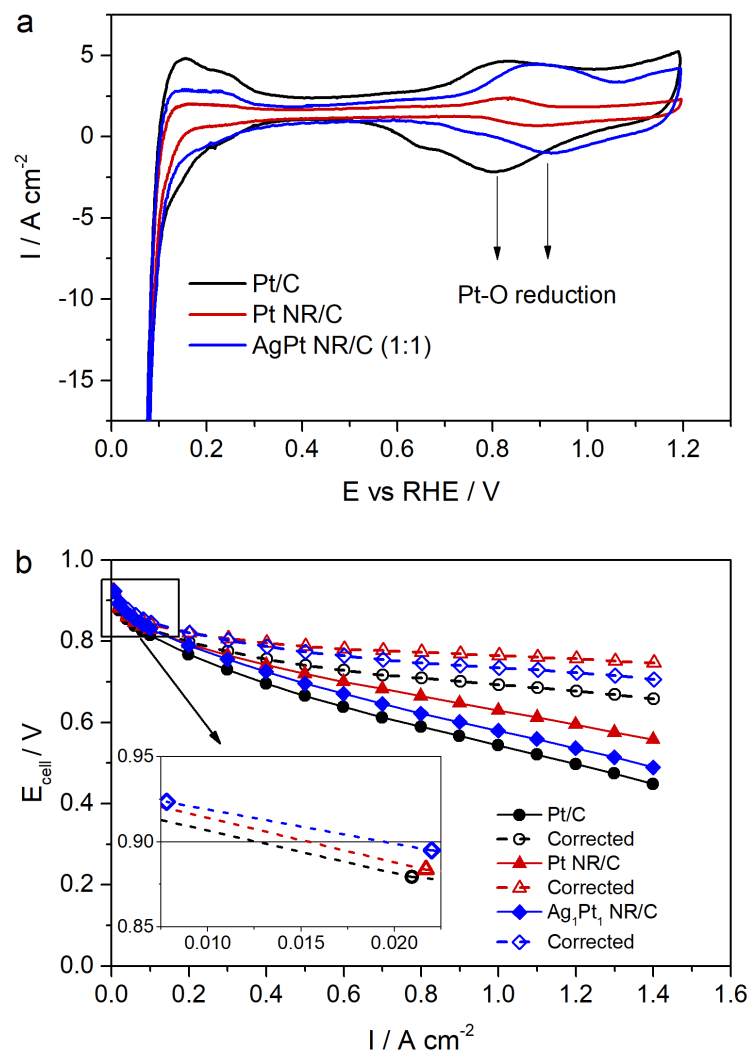


Fig. 6 a) Cathode CVs recorded between 0.05-1.2 V with a scan rate of $20\ mV\ s^{-1}$ (the cathode is saturated with N_2) and **b)** polarization curves obtained under H_2/O_2 testing at a pressure of 1.5/1.5 bar with stoichiometry ratios of 2/9.5, respectively. The inset compares the current density at around 0.9 V. The measurements were recorded at a cell temperature of $80\ ^\circ C$ with fully humidified gases.

The mass activity of the Ag_1Pt_1 NR/C catalyst towards ORR in the MEA was evaluated under O_2 with a high stoichiometry of 9.5 as defined by the U.S. DOE to minimize the influence of mass

transport, and the recorded polarization curve was corrected with the ohmic resistance loss and H₂-crossover (**Fig. 6b**). The corresponding mass activity (MA) of the catalysts are summarized in **Table 1**. The current density recorded at 0.9 V is 0.019 A cm⁻² for Ag₁Pt₁ NR/C, much higher than 0.013 and 0.016 A cm⁻² for Pt/C and Pt NR/C, respectively. Normalized to the Pt loading, Ag₁Pt₁ NR/C shows 1.22 and 1.51 fold of mass activities over Pt NR/C and Pt/C, respectively, signifying the enhancement for a better ORR activity by alloying Pt with Ag. At the high current density region above 0.3 A cm⁻², due to the reduced mass transport losses resulting from the longer NRs⁸, better power performance is achieved for Pt NR/C compared to Ag₁Pt₁ NR/C. The Tafel slopes based on the three polarization curves (Figure 6b) plots are indicated in Fig. S11. Because this measurement is conducted within MEAs, not as the pure environment as that with half-cell measurement by the rotating disk electrode (RDE) technique in liquid electrolyte, so the influence of mass transfer cannot be fully mitigated. The obtained slope for Pt/C is 75 mV dec⁻¹, which is still in a close agreement with the value report in literature⁴². The lowest slope of 68 mV dec⁻¹ is found for the MEA with the Pt NR/C catalysts resulting from the improved mass transport owing to the long NRs. The Ag₁Pt₁ NR/C catalyst generates a Tafel slope of 72 mV dec⁻¹, indicating more favorable ORR kinetics as compared to 0D Pt/C, but still higher than the long Pt NRs³². Thus, optimizing the approach to obtain uniformly longer 1D AgPt alloy based catalysts is important for the future work.

Table 1. Comparison of the mass activities for the catalysts in the MEA test

Catalyst	$I_{0.9\text{V}} / \text{A cm}^{-2}$	$\text{MA}_{0.9\text{V}} / \text{A mg}_{\text{Pt}}^{-1}$
Pt/C	0.013	0.065
Pt NR/C	0.016	0.080

In acidic media as in PEMFCs, the only reaction pathway observed for Ag is limited two-electron reduction resulting in a very low ORR catalytic activity⁴³. Together with the nearly ignorable cost of Ag (*cf.* Pt), so the mass activity normalized to Pt is highly sensible in practical application, with which Ag₁Pt₁ NR/C exhibits strong superiority.

The enhancement in the catalytic activity towards ORR is related to the modified Pt surface, deriving mainly from the 1D structure and the involvement of the alloyed Ag. The formation of single-crystal along the <111> direction facilitates a preferential exposure of the highly active crystal facets with the improved ORR activities⁹. Cathode CV plots in **Fig. 6a** shows a positive shift of the Pt-O reduction peak for Pt NR/C at 0.889 V as compared to 0.805 V for Pt/C. This shift (0.084 V) indicates the weakening bond of the O-containing species on the smooth atomic surface of 1D NRs, which is expected to contribute to the enhanced ORR activity⁴⁴. This improvement is boosted by the synergy effect between Ag and Pt interaction in the alloy form. The introduction of Ag induces more positive shift as observed from the Ag₁Pt₁ NR/C catalyst (**Fig. 6a**), for which the Pt-O reduction peak position is 0.913 V (with a shift of 0.108 V), indicating a higher ORR catalytic performance compared to Pt NR/C catalyst. The alloy causes a tensile strain on the Pt lattice because of the different lattice constants of Pt and Ag (3.92 and 4.09 Å, respectively), changing the Pt d-band center and modifying the electronic structure, which is confirmed by the XPS analysis (**Fig. 4**)^{45,46}. These changes lead to weaker binding of Pt surface with O-containing species formed in the ORR process, thus facilitating the desorption of oxygen for the increased ORR kinetic⁴⁷. Furthermore, the fewer surface defects of NRs (*cf.* NPs) also contributes to the less interaction with O-contained species. Therefore, a good balance of Ag and Pt in the alloyed

NR catalysts (i.e. Ag_1Pt_1 NR/C) provides a harmony of the O-H bonding formation and O-O bonding cleavage, finally leading to the enhanced catalytic activities.

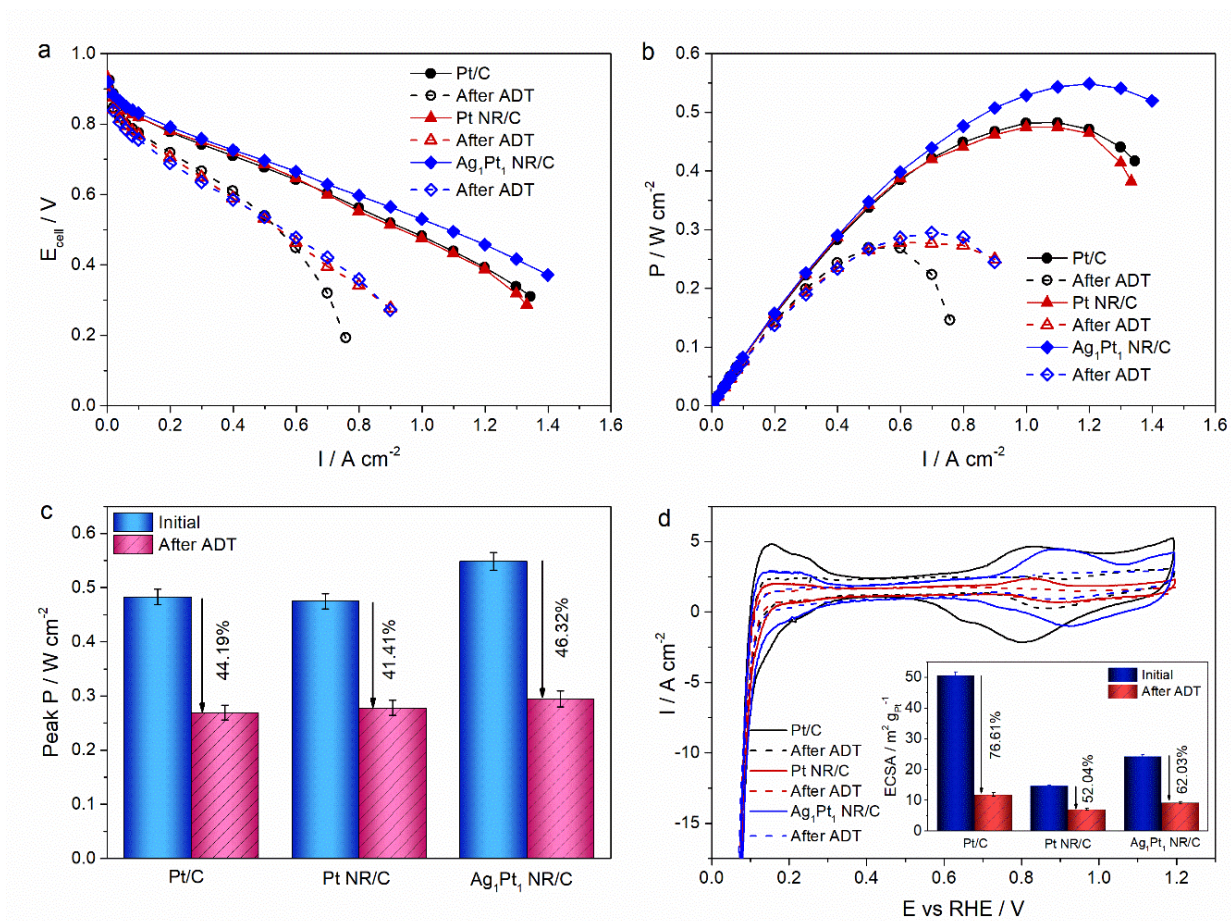


Fig. 7 Comparison of the Pt/C, Pt NR/C and Ag_1Pt_1 NR/C cathodes after the ADT using 5000 potential sweeping cycles in the MEA test: **a)** polarization and **b)** power density curves, **c)** peak power density showing the declines after the ADT, **d)** cathode CVs and corresponding ECSA declines after the ADT.

Besides the low ORR activity, Ag is also commonly reported with low stability in the acidic environment⁴⁸, so the durability of the Ag_1Pt_1 NR/C cathode is further examined using accelerated durability test (ADT) in the single-cell test. The polarization and power density curves after the ADT are shown in **Fig. 7a-b**. The MEA with the Ag_1Pt_1 NR/C cathode still demonstrates the

highest peak power density after the ADT compared to Pt/C and Pt NR/C. However, it exhibits a slightly higher decline rate of 46.32% compared to 44.19% and 41.41% for two others, respectively (**Fig. 7c**, the error bar was obtained considering the fluctuation of the potential obtained in repeat experiments while holding at the same current density). The immense power performance loss of the Ag₁Pt₁ NR/C catalyst after the ADT is addressed to the dissolution of Ag, as shown in Fig. S12. Regardless of a close lattice constant of Ag and Pt, nevertheless, the segregation of Ag cannot be avoided in the severe acidic environment in the PEMFCs operation condition⁴⁹. Finally, it leads to redeposition of Ag at the interface between the cathode and electrolyte membrane inducing a huge performance drop after the ADT.

The surface area loss also contributes to the power performance decline after the ADT, which is shown by the CV analysis and the corresponding ECSA change in **Fig. 7d**. Ag₁Pt₁ NR/C exhibits a declining ratio of 62.03%, much smaller than 76.61% of Pt/C, but higher than 52.04% of Pt NR/C (**Fig. 7d**). These indicate better stability of Ag₁Pt₁ NR/C than Pt/C and reasonable electrode durability for applications in practical devices. In addition, the significant loss observed can potentially be contributed also to the corrosion of the carbon support in potential cycling, which induces severe degradation of the catalysts and this challenge has been extensively reviewed in literature^{44,50}. Therefore, the elimination of carbon support for developing 1D alloy catalyst should be considered for future works, such as electrodes with self-stand 1D alloy nanostructure arrays.

Conclusions

In this work, an efficient approach for growing AgPt alloy nanorods on carbon support is demonstrated. The morphology characterization showed that the time interval (i.e. 5 hours) of mixing both metal precursors is a crucial step to achieve uniform 1D nanostructures. In the formic

acid reduction process, Pt works not only a size control role in Ag reduction, but also providing shape inducing effect leading the growth of AgPt alloy to form single-crystal nanorods along the $\langle 111 \rangle$ direction. The atomic ratio of Ag to Pt (from 1:4 to 2:1) affects a change on the morphology and distribution of AgPt NRs on the carbon support, which also delivers an enormous impact on their catalytic activities. The MEA test in PEMFCs shows an enhanced power density of 0.549 W cm^{-2} for the AgPt alloy catalyst due to the superiority of 1D metal nanostructure and high electrical conductivity of Ag, which is 1.14- and 1.16-fold over that of Pt/C and Pt NR/C, and the mass activity tested under oxygen is 1.51- and 1.22-fold higher, respectively. The ADT testing also convinces that alloying Pt with Ag (atomic ratio of Ag:Pt = 1:1) in NRs is less an issue towards the stability under the harsh operational conditions in fuel cell operation, although slightly lower compared to 1D Pt NR, but better than 0D Pt NP.

Electronic Supplementary Information

HRTEM images and STEM-EDX analysis of Ag_1Pt_4 NR/C, TEM images of AgPt NR/C with varied atomic ratio. The quantitative result obtained from TGA, ICP-MS and EDX with the EDX spectrum of AgPt NR/C with varied atomic ratio. Additional XRD pattern for Ag_2Pt_1 NR/C -ii, TEM images of Ag_1Pt_1 NR/C with different annealing temperature. XPS survey with the table summarizing the composition state of the as-made catalysts. EIS spectra measured at 0.5 V of the as-prepared catalysts and additional MEA testing result due to heat treatment effect with corresponding EIS measured at 0.03 A cm^{-2} and 0.5 V and XPS spectra of Ag_1Pt_1 NR/C. The cathode CVs of the as-prepared catalysts and corresponding measured ECSA and Pt-O reduction

peak. The Tafel plot and the cross-sectional SEM-EDX mapping of Ag/Pt, NR/C after the ADT. This material is available free of charge via the Internet at <http://pubs.rsc.org>.

Conflicts of interest

There are no conflicts to declare.

Acknowledgement

This work is part of E. Fidiani PhD studentship sponsored by the Indonesian Endowment Fund for Education (LPDP) and the EPSRC Centre for Doctoral Training in Fuel Cells and their Fuels (EP/L015749/1).

References

- 1 N. Jung, D. Y. Chung, J. Ryu, S. J. Yoo and Y. E. Sung, *Nano Today*, 2014, 9, 433–456.
- 2 A. Morozan, B. Josselme and S. Palacin, *Energy Environ. Sci.*, 2011, 4, 1238–1254.
- 3 V. Mazumder, Y. Lee and S. Sun, *Adv. Funct. Mater.*, 2010, 20, 1224–1231.
- 4 J. C. Meier, C. Galeano, I. Katsounaros, J. Witte, H. J. Bongard, A. A. Topalov, C. Baldizzone, S. Mezzavilla, F. Schüth and K. J. J. Mayrhofer, *Beilstein J. Nanotechnol.*, 2014, 5, 44–67.
- 5 B. Li, Z. Yan, D. C. Higgins, D. Yang, Z. Chen and J. Ma, *J. Power Sources*, 2014, 262,

- 488–493.
- 6 B. Li, D. C. Higgins, Q. Xiao, D. Yang, C. Zhng, M. Cai, Z. Chen and J. Ma, *Appl. Catal. B Environ.*, 2015, **162**, 133–140.
 - 7 Z. Chen, M. Waje, W. Li and Y. Yan, *Angew. Chemie - Int. Ed.*, 2007, **46**, 4060–4063.
 - 8 P. Mardle, X. Ji, J. Wu, S. Guan, H. Dong and S. Du, *Appl. Catal. B Environ.*, , DOI:10.1016/j.apcatb.2019.118031.
 - 9 C. Koenigsmann and S. S. Wong, *Energy Environ. Sci.*, 2011, **4**, 1161–1176.
 - 10 J. N. Tiwari, R. N. Tiwari and K. S. Kim, *Prog. Mater. Sci.*, 2012, **57**, 724–803.
 - 11 Y. Lu, S. Du and R. Steinberger-Wilckens, *Appl. Catal. B Environ.*, 2016, **199**, 292–314.
 - 12 V. Čolić and A. S. Bandarenka, *ACS Catal.*, 2016, **6**, 5378–5385.
 - 13 S. Tang, S. Vongehr, Z. Zheng and X. Meng, *J. Colloid Interface Sci.*, 2010, **351**, 217–224.
 - 14 S. G. Peera, T. G. Lee and A. K. Sahu, *Sustain. Energy Fuels*, 2019, **3**, 1866–1891.
 - 15 V. Stamenkovic, B. S. Mun, K. J. J. Mayrhofer, P. N. Ross, N. M. Markovic, J. Rossmeisl, J. Greeley and J. K. Nørskov, *Angew. Chem. Int. Ed. Engl.*, 2006, **45**, 2897–901.
 - 16 V. R. Stamenkovic, B. Fowler, B. S. Mun, G. Wang, P. N. Ross, C. A. Lucas and N. M. Markovic, *Science (80-.)*, 2007, **315**, 493–497.
 - 17 D. Y. Chung, S. W. Jun, G. Yoon, S. G. Kwon, D. Y. Shin, P. Seo, J. M. Yoo, H. Shin, Y. H. Chung, H. Kim, B. S. Mun, K. S. Lee, N. S. Lee, S. J. Yoo, D. H. Lim, K. Kang, Y. E. Sung and T. Hyeon, *J. Am. Chem. Soc.*, 2015, **137**, 15478–15485.

- 18 D. Wang, H. L. Xin, R. Hovden, H. Wang, Y. Yu, D. A. Muller, F. J. Disalvo and H. D. Abruña, *Nat. Mater.*, 2013, **12**, 81–87.
- 19 R. Borup, J. Meyers, B. Pivovar, Y. S. Kim, R. Mukundan, N. Garland, D. Myers, M. Wilson, F. Garzon, D. Wood, P. Zelenay, K. More, K. Stroh, T. Zawodzinski, J. Boncella, J. E. McGrath, M. Inaba, K. Miyatake, M. Hori, K. Ota, Z. Ogumi, S. Miyata, A. Nishikata, Z. Siroma, Y. Uchimoto, K. Yasuda, K. I. Kimijima and N. Iwashita, *Chem. Rev.*, 2007, **107**, 3904–3951.
- 20 F. Maillard, L. Dubau, J. Durst, M. Chatenet, J. André and E. Rossinot, *Electrochem. commun.*, 2010, **12**, 1161–1164.
- 21 Q. Cui, Y. Zhang and Z. Peng, *Chem. Res. Chinese Univ.*, 2016, **32**, 106–111.
- 22 M. Chatenet, L. Genies-Bultel, M. Aurousseau, R. Durand and F. Andolfatto, *J. Appl. Electrochem.*, 2002, **32**, 1131–1140.
- 23 Y. T. Liang, S. P. Lin, C. W. Liu, S. R. Chung, T. Y. Chen, J. H. Wang and K. W. Wang, *Chem. Commun.*, 2015, **51**, 6605–6608.
- 24 X. Cao, N. Wang, Y. Han, C. Gao, Y. Xu, M. Li and Y. Shao, *Nano Energy*, 2015, **12**, 105–114.
- 25 A. J. Wang, L. Liu, X. X. Lin, J. Yuan and J. J. Feng, *Electrochim. Acta*, 2017, **245**, 883–892.
- 26 F. Q. Shao, X. Y. Zhu, A. J. Wang, K. M. Fang, J. Yuan and J. J. Feng, *J. Colloid Interface Sci.*, 2017, **505**, 307–314.

- 27 I. E. L. Stephens, A. S. Bondarenko, U. Grønbjerg, J. Rossmeisl and I. Chorkendorff, *Energy Environ. Sci.*, 2012, **5**, 6744–6762.
- 28 M. Wang, H. Zhang, G. Thirunavukkarasu, I. Salam, J. R. Varcoe, P. Mardle, X. Li, S. Mu and S. Du, *ACS Energy Lett.*, 2019, **4**, 2104–2110.
- 29 K. M. Koczkur, S. Mourdikoudis, L. Polavarapu and S. E. Skrabalak, *Dalt. Trans.*, 2015, **44**, 17883–17905.
- 30 H. Meng, Y. Zhan, D. Zeng, X. Zhang, G. Zhang and F. Jaouen, *Small*, 2015, **11**, 3377–3386.
- 31 S. Du, *Int. J. Low-Carbon Technol.*, 2012, **7**, 44–54.
- 32 Y. Lu, S. Du and R. Steinberger-Wilckens, *Appl. Catal. B Environ.*, 2015, **164**, 389–395.
- 33 A. Boronat-González, E. Herrero and J. M. Feliu, *J. Solid State Electrochem.*, 2014, **18**, 1181–1193.
- 34 K. Kinoshita, K. Routsis and J. A. S. Bett, *Thermochim. Acta*, 1974, **10**, 109–117.
- 35 C. J. Levy and R. J. Puddephatt, *Organometallics*, 1997, **16**, 4115–4120.
- 36 S. Du, K. Lin, S. K. Malladi, Y. Lu, S. Sun, Q. Xu, R. Steinberger-Wilckens and H. Dong, *Sci. Rep.*, , DOI:10.1038/srep06439.
- 37 A. Bin Yousaf, M. Imran, A. Zeb, T. Wen, X. Xie, Y. F. Jiang, C. Z. Yuan and A. W. Xu, *Electrochim. Acta*, 2016, **197**, 117–125.
- 38 H. Liu, F. Ye, Q. Yao, H. Cao, J. Xie, J. Y. Lee and J. Yang, *Sci. Rep.*, 2014, **4**, 1–7.

- 39 C. Fang, J. Zhao, G. Zhao, L. Kuai and B. Geng, *Nanoscale*, 2016, **8**, 14971–14978.
- 40 D. R. Lide, G. Baysinger, L. I. Berger, R. N. Goldberg, H. V Kehiaian, K. Kuchitsu, D. L. Roth and D. Zwillinger, *CRC Handbook of Chemistry and Physics Editor-in-Chief*, .
- 41 K. S. Moon, H. Dong, R. Maric, S. Pothukuchi, A. Hunt, Y. I. Li and C. P. Wong, *J. Electron. Mater.*, 2005, **34**, 168–175.
- 42 H. A. Gasteiger, S. S. Kocha, B. Sompalli and F. T. Wagner, *Appl. Catal. B Environ.*, 2005, **56**, 9–35.
- 43 B. B. Blizanac, P. N. Ross and N. M. Markovic, *Electrochim. Acta*, 2007, **52**, 2264–2271.
- 44 S. Sun, G. Zhang, D. Geng, Y. Chen, R. Li, M. Cai and X. Sun, *Angew. Chemie - Int. Ed.*, 2011, **50**, 422–426.
- 45 Z. Peng, H. You and H. Yang, in *Advanced Functional Materials*, 2010, vol. 20, pp. 3734–3741.
- 46 T. Fu, J. Fang, C. Wang and J. Zhao, *J. Mater. Chem. A*, 2016, **4**, 8803–8811.
- 47 M. P. Hyman and J. W. Medlin, *J. Phys. Chem. C*, 2007, **111**, 17052–17060.
- 48 H. A. Hansen, J. Rossmeisl and J. K. Nørskov, *Phys. Chem. Chem. Phys.*, 2008, **10**, 3722–3730.
- 49 Y. Ma and P. B. Balbuena, *Surf. Sci.*, 2008, **602**, 107–113.
- 50 S. Holdcroft, *Chem. Mater.*, 2014, **26**, 381–393.